small
www.small-journal.com

Electrochemical Biosensor Composed of Silver Ion-Mediated dsDNA on Au-Encapsulated Bi_2Se_3 Nanoparticles for the Detection of H_2O_2 Released from Breast Cancer Cells

Mohsen Mohammadniaei, Jinho Yoon, Taek Lee, Bapurao G. Bharate, Jinhee Jo, Donghyun Lee, and Jeong-Woo Choi**

A newly developed electrochemical biosensor composed of a topological insulator (TI) and metallic DNA (mDNA) is fabricated. The bismuth selenide nanoparticle (Bi_2Se_3 NP) is synthesized and sandwiched between the gold electrode and another Au-deposited thin layer (Bi_2Se_3@Au). Then, eight-silver-ion mediated double-stranded DNA (mDNA) is immobilized onto the substrate (Bi_2Se_3@Au-mDNA) for the further detection of hydrogen peroxide. The Bi_2Se_3 NP acts as the electrochemical-signal booster, while unprecedentedly its encapsulation by the Au thin layer keeps the TI surface states protected, improves its electrochemical-signal stability and provides an excellent platform for the subsequent covalent immobilization of the mDNA through Au–thiol interaction. Electrochemical results show that the fabricated biosensor represents much higher Ag^+ redox current (≈10 times) than those electrodes prepared without Bi_2Se_3@Au. The characterization of the Bi_2Se_3@Au-mDNA film is confirmed by atomic force microscopy, scanning tunneling microscopy, and cyclic voltammetry. The proposed biosensor shows a dynamic range of 00.10×10^{-6} M to 27.30×10^{-6} M, very low detection limit (10×10^{-9} M), unique current response (1.6 s), sound H_2O_2 recovery in serum, and substantial capability to classify two breast cancer subtypes (MCF-7 and MDA-MB-231) based on their difference in the H_2O_2 generation, offering potential applications in the biomedicine and pharmacology fields.

1. Introduction

The electrochemical biosensors are the powerful analytical devices in the numerous fields of medicine, environmental monitoring, food analysis, and diagnosis owing to their simplicity, fast response, low cost, and high sensitivity.[1] Hydrogen peroxide (H_2O_2), an important biomarker of the major reactive oxygen species, is related to various bodily disorders including asthma, Alzheimer's disease, cancer, and inflammatory arthritis;[2,3] therefore, a rapid and selective detection of the H_2O_2 level at a very low concentration is demanding. Various detection methods have been developed such as chromatography,[4] titrimetry,[5] chemiluminescence,[6] spectrophotometry,[7] ferrous oxidation-xylenol orange assay,[8] and electrochemistry.[9] Among them, enzyme-based electrochemical H_2O_2 biosensors are demonstrated as the most suitable and effective tools owing to their low cost, simple design, high sensitivity, and selectivity; however, they are still restricted to complicated immobilization process and relatively low stability.[10,11] It has been proved that the incorporation of biomolecules such as metalloproteins with nanostructured solid electrodes can amplify the electron-transfer rate between the nanobiofilm and the solution interface, giving rise to the development of several sensitive electrochemical biosensors.[12–15] Although, despite the 3D structure of metalloprotein that results in its effective immobilization onto the solid electrodes, the number of metal ions (electroactive prosthetic groups) is limited to the number of proteins.

For the development of high-performance H_2O_2 biosensors, the employment of an electrode with a large effective area, a high electron conductivity to facilitate the interfacial charge transfer, and a robust stability for the provision of reliable results are crucial. Several types of nanomaterials including the transition metals,[16] carbon nanotube,[17] and graphene[18] have been used for the electrocatalytic detection of H_2O_2 due to their large surface-to-volume ratio and remarkable electrical and electrochemical properties. Recently, as newly emerged exotic materials, topological insulators (TIs) have attracted intensive interest from various interdisciplinary research fields.[19–21] Due to their strong spin-orbit coupling, TIs represent a new phase of quantum matters with semiconducting bulk and surface states

M. Mohammadniaei, J. Yoon, Dr. B. G. Bharate, J. Jo, Prof. J.-W. Choi
Department of Chemical and Biomolecular Engineering
Sogang University
35 Baekbeom-ro (Sinsu-dong), Mapo-gu, Seoul 121-742, Republic of Korea
E-mail: jwchoi@sogang.ac.kr
Prof. T. Lee
Department of Chemical Engineering
Kwangwoon University
20 Kwangwoon-Ro, Nowon-Gu, Seoul 01897, Republic of Korea
Prof. D. Lee
School of Integrative Engineering
Chung-Ang University
Heukseok-dong, Dongjak-gu, Seoul 156-756, Republic of Korea
E-mail: dhlee@cau.ac.kr

DOI: 10.1002/smll.201703970

or conducting edges, and they are immune to small time-reversal perturbations such as backscattering, crystal disorders, and nonmagnetic impurities.[22–24] The TI surface states provide a 2D Dirac system out of a bulk material that is observed in only the graphene atomic monolayer.[25] Also, the preservation of the electron-state coherence up to room temperature have made these materials serious rivals for graphene.[25]

Bismuth selenide (Bi_2Se_3), a so-called 3D TI, has exhibited very promising properties like Dirac plasmons,[25] thermoelectric behavior,[26] photothermal-conversion ability,[27] and unique electrical conductivity because of the existence of a single-surface Dirac cone and a six-valley degeneracy.[28,29] Possessing a sound biocompatibility, Bi_2Se_3 has been employed for clinical applications such as cancer radiation therapy and imaging,[30,31] as well as biomarker detection and diagnosis in the forms of nanoparticles (NPs) and nanosheets.[32–34] Bi_2Se_3 has also shown significant electrochemical catalytic properties that provides a highly effective platform for the development of different types of electrochemical biosensors.[33] An electrochemical-signal enhancement with the aim of reducing the background signal and increasing the reproducibility is vital for biosensors for the precise detection of biomarkers. It is worth noting that, the TI capability for the suppression of the backscattering and the fluctuation of the spin-polarized charge that is carried on the surface states[35] could lower the electronic noise,[36] thereby resulting in a signal-to-noise ratio enhancement for the development of credible TI-based biosensors with very low detection limits. Although, with major nanotechnology support, the TI properties have been boosted remarkably,[37–40] but the direct utilization of the TIs into biotechnological applications is still challenging because of the difficulties regarding the surface functionalization and the necessity to increase their sensitivity and fidelity. Consequently, the encapsulation of these materials with other types of inorganic or organic materials seems demanding.[41]

Up until the present study, only a few studies have been performed for the H_2O_2 detection that is based on TI-biomolecule hybrids. Regarding H_2O_2 detection, the high-sensitivity values of 3D flower-like molybdenum disulfide (MoS_2)/hemoglobin[42] and hemoglobin-mediated flower-like Bi_2Se_3[43] have been reported; although, they are limited by a high detection limit, narrow dynamic range, high response time (>10 s), and low biomolecule-conjugation efficiency. Recently, MoS_2-encapsulated graphene oxide was also reported by the authors regarding an amplification of the H_2O_2-detection process that is based on the redox behavior of the myoglobin.[41] A more detailed comparison that is besides a number of the notable reported studies is also provided in Table S1 (Supporting Information).

To address the previously mentioned issues, an ultra-fast, sensitive, simply designed, and reliable H_2O_2 biosensor composed of a Bi_2Se_3-sandwiched Au thin film (Bi_2Se_3@Au) that has been immobilized by metallic DNA (mDNA) is presented here, which is subsequently called Bi_2Se_3@Au-mDNA in this article. The mDNA consisted of an optimized eight-Ag^+-inserted dsDNA (C-8Ag^+-C) which compared to the metalloproteins, each mDNA harbored eight metal ions to offer higher sensitivity and stability. It should be noted that, Ag^+ ion can be easily intercalated between the cytosine–cytosine (C-C) mismatches of the DNA duplex to stabilize the structure.[44] Also for the first time, synthesized Bi_2Se_3 NPs as the electrochemical-signal enhancers were sandwiched between the gold electrode surface and a thin layer of thermal-evaporated Au. This resulted in robustness enhancement of the electrode to avoid Bi_2Se_3 NPs dissolution into the electrolyte followed by an excellent reproducible electrochemical signal, also, provided a nanostructured surface with a high porosity, whereby its readiness for the Au–thiol covalent bonding between the electrode and the biomolecules was established. In addition, with the help of scanning tunneling spectroscopy (STS) analysis, we observed that the thickness of Au deposited thin layer had a big impact on the retaining of Bi_2Se_3 surface states which enabled us to keep the peculiar electrochemical features of Bi_2Se_3 NPs. The mDNA was immobilized onto the substrate through the Au–thiol interaction, thereby offering a discrete electrochemical signal that is the result of the H_2O_2 reduction caused by the reversible conversion of Ag^{2+} to Ag^+. An unprecedented ultrafast response time of 1.6 s, along with a very low detection limit of 10×10^{-9} M, was observed on the fabricated electrode. The fast current response, however, could be ascribed to the sharp redox signals of the Ag^+ ion and the low ΔE_p of 66 mV that resulted in a high electron-transfer rate across the structures; also, the Bi_2Se_3 NPs played a significant role in the repression of the backscattering effects of the charge carriage, as well as the increasing of the charge mobility between the interfaces. The developed biosensor also showed a sound H_2O_2 recovery (98.1% to 103.6%) in serum with a remarkable ability to distinguish between two breast cancer subtypes (MCF-7 and MDA-MB-231) based on the amount of H_2O_2, generated by each cell lines upon the phorbol 12-myristate 13-acetate (PMA) induction. In this study, cyclic voltammetry (CV) and amperometric (*i–t*) techniques were used for the measurements of the electrocatalytic reduction of H_2O_2. **Figure 1** shows the synthesis and analysis methods of the Bi_2Se_3@Au electrode (upper panel) and the proposed Bi_2Se_3@Au-mDNA biosensor performance (bottom panel).

2. Results and Discussions

2.1. Conformation Analysis of the Synthesized Bi_2Se_3 Nanoparticles

A morphological study of the as-prepared Bi_2Se_3 NPs was investigated using transmission electron microscopy (TEM) (**Figure 2**a,b). The size and shape of the NPs were determined from the TEM image of the as-synthesized Bi_2Se_3 NPs. The high-resolution TEM image (Figure 2c) confirmed the presence of hexagonal lattice fringes of Bi_2Se_3 NPs with the lattice spacing of 0.208 nm corresponding to the [110] planes. Also energy dispersive X-ray spectroscopy (EDS) mapping in Figure 2c reveals a well distribution of Bi and Se inside the NP structure. The EDS analysis of the Bi_2Se_3 NPs in Figure S1 (Supporting Information) also indicates that only Bi and Se can be detected besides the C, Cu, and Cr signals in the grid that is used for the TEM measurement. The atomic ratio of the Bi and Se was 0.4:0.6, which is very close to the Bi_2Se_3 phase.

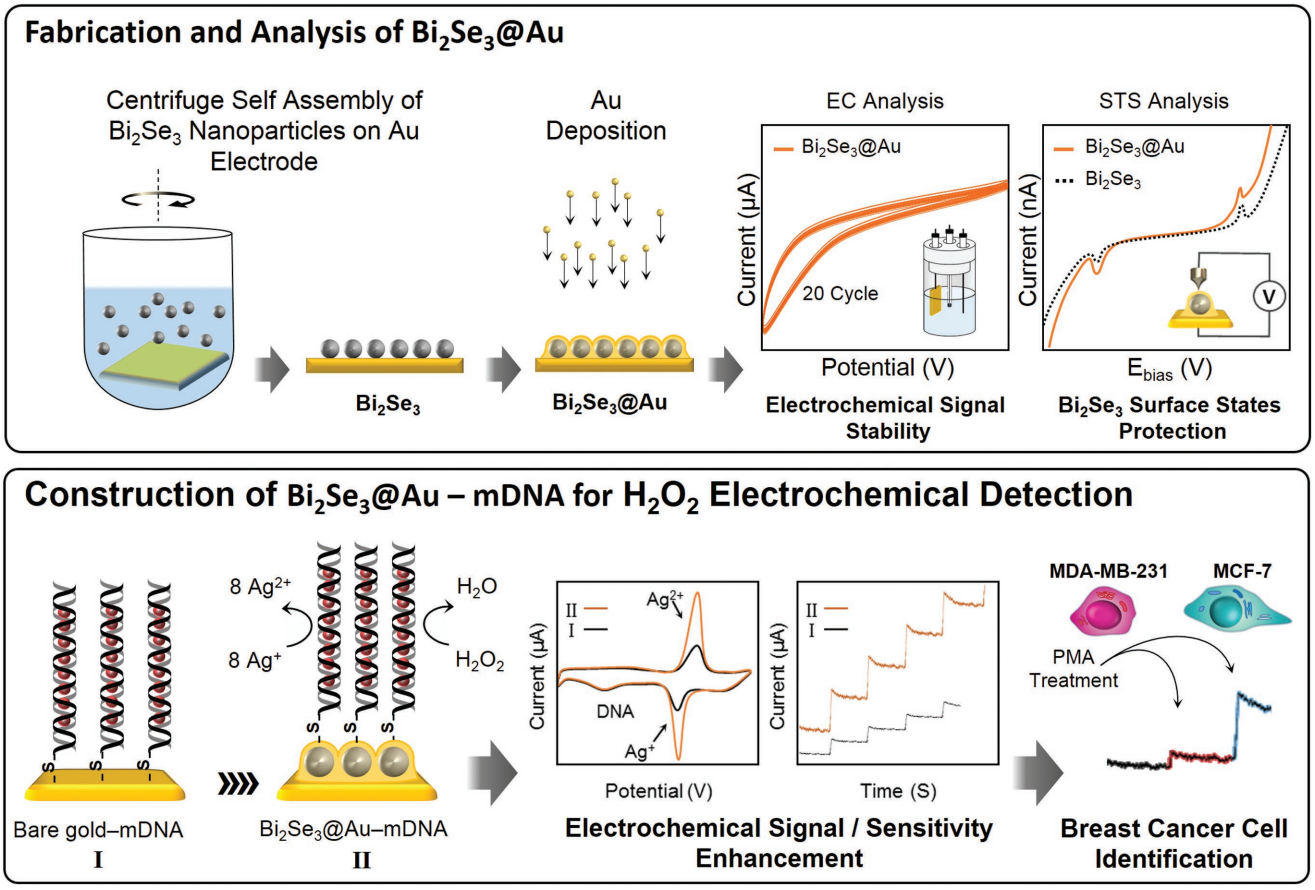

Figure 1. Schematic diagram of the fabrication process of Bi_2Se_3@Au-mDNA electrode, and its electrical and electrochemical behavior and the constitution for the electrochemical detection of H_2O_2.

The measurement of the particle-size distribution of the sonicated Bi_2Se_3 nanocrystals was performed using dynamic light-scattering technique via a laser-input energy of 632 nm (Figure 2d). The as-prepared sample showed a wide size distribution, and its particle distribution that is between 16 and 35 nm comprises an average distribution of 23.06 nm.

Figure 2e shows the X-ray powder diffraction (XRD) pattern of the as-prepared Bi_2Se_3 NPs, where all of the diffraction peaks can be readily indexed to the hexagonal structure of the Bi_2Se_3, which is in a good agreement with the literature values (JCPDS 33-0214). The XRD pattern of the as-synthesized Bi_2Se_3 NPs shows major peaks at the 2Θ values of 29.2, 44.2, 53.8, 72.2, and 78.5 that correspond to the reflections of the (015), (110), (205), (125), and (2110) planes, respectively. For the other impurities, characteristic peaks are not evident, indicating a high product purity.

The optical-absorption spectra of the Bi_2Se_3 have been studied at room temperature in the wavelength region of 300–850 nm. Figure 2f shows the optical-absorption spectrum of the Bi_2Se_3-NP suspensions in the water–dimethylformamide mixture. The absorption for the as-prepared Bi_2Se_3 NPs was found in the region of 450–470 nm, resulting in a band gap of >2.7 eV, which is similar to those that have been reported for the Bi_2Se_3 NPs.

2.2. Surface Characterization of the Layer-by-Layer Formation of the Bi_2Se_3@Au-mDNA Using Atomic Force Microscopy (AFM) and Electrochemical Impedance Spectroscopy (EIS)

Prior to the surface characterization, the successful formations of DNA duplexes were tested by performing polyacrylamide gel electrophoresis and melting temperature analysis; from which the duplexes with eight C–Ag+–C modification (mDNA) were observed to be more stable (details in Section S.1 and Figure S2, Supporting Information). The structure formation of the Bi_2Se_3@Au electrode and the further immobilization of the mDNA were confirmed using AFM and EIS methods (**Figure 3**). As shown in Figure 3, a clear discrimination is presented between the bare-Au electrode (Figure 3a) and the Au electrode after the Bi_2Se_3 NPs assembly (Figure 3b). The blurry morphological image that is evident in Figure 3c is a result of the thermal evaporation of a few Au nanometers for 10 min onto the Bi_2Se_3 NPs following an increase of the lateral sizes of NPs. Figure 3d illustrates the topological image of the whole fabricated biosensor structure in which the mDNA is effectively immobilized on the Bi_2Se_3@Au film due to the Au–thiol bonding.

The EIS measurement was also employed in order to further investigate the layer-by-layer formation of Bi_2Se_3@Au-mDNA

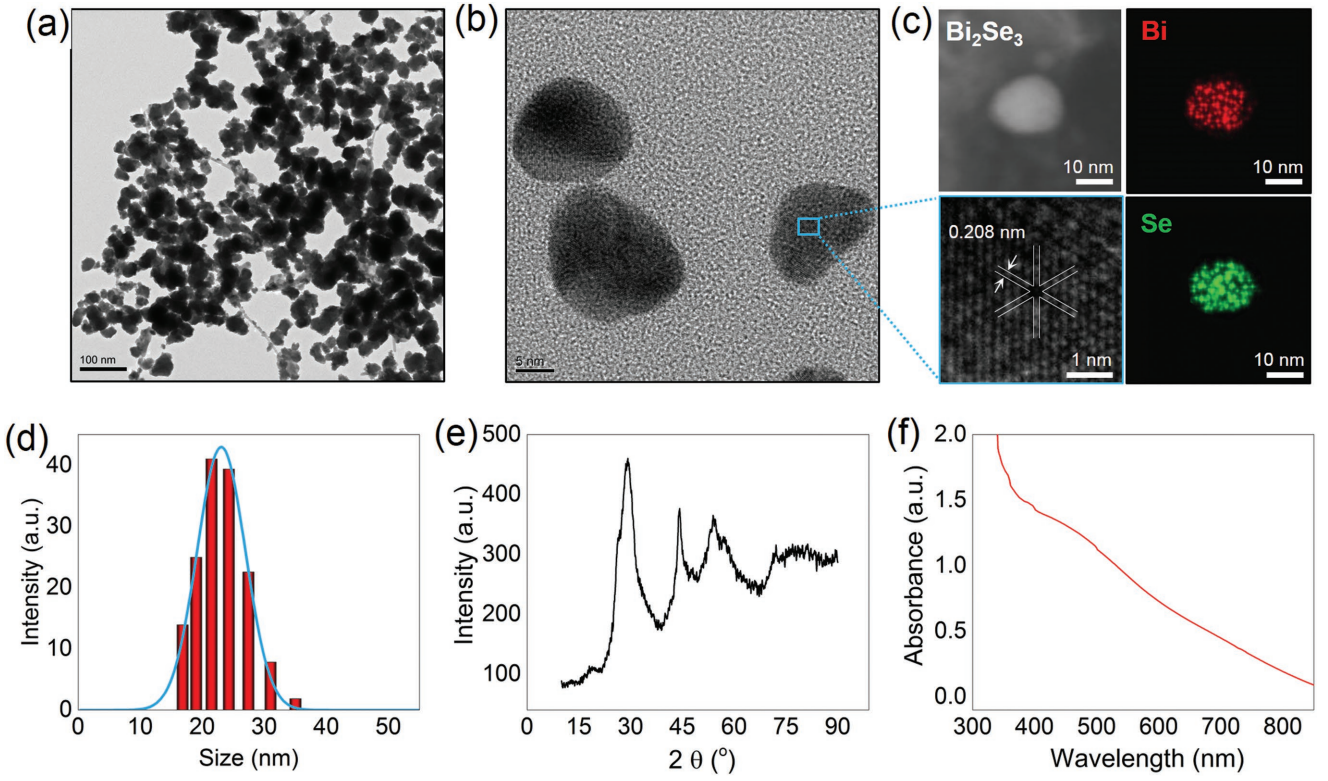

Figure 2. Conformation analysis of the Bi_2Se_3 NPs. a) TEM image, b) high-resolution TEM image, c) EDS mapping images of Bi_2Se_3 NP and high magnitude TEM image for the lattice structure analysis, d) particle size distribution, e) XRD pattern, and f) UV–vis spectra of the as-prepared Bi_2Se_3 NPs.

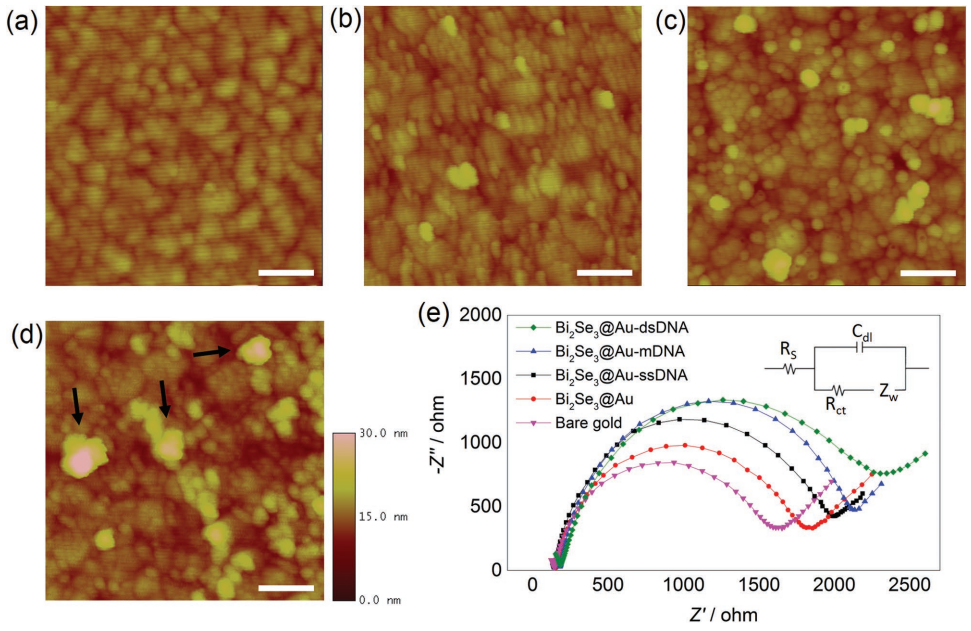

Figure 3. Structure characterization of the nanobiofilm. AFM picture of a) bare gold electrode, b) Bi_2Se_3 centrifuge assembled on bare gold, c) Bi_2Se_3 centrifuge assembled on bare gold following by Au deposition (Bi_2Se_3@Au) using physical vapor deposition method for 10 min, d) 8 silver ions intercalated DNA (mDNA) which is self-assembled on Bi_2Se_3@Au to become Bi_2Se_3@Au-mDNA; black arrows show the location of DNAs; Scale bar: 200 nm; e) Nyquist plots (Z′ vs. –Z″) obtained for bare gold electrode, Bi_2Se_3@Au, Bi_2Se_3@Au-ssDNA, Bi_2Se_3@Au-mDNA, and Bi_2Se_3@Au-dsDNA; the inset shows the Randles equivalent circuit model. All the experiments were performed in PBS buffer (pH 7.4) containing 5×10^{-3} M $Fe(CN)_6^{4-/3-}$.

electrode. EIS is an effective method for the characterization of self-assembly monolayer of biomolecules onto the electrodes and to better understand the electron transfer kinetics between the interfaces during the modification process. The semicircular diameter of the Nyquist plot at higher frequencies corresponds to the charge-transfer resistance (R_{ct}) and the variation of R_{ct} is attributed to the different modifications of electrodes (Figure 3e). For our experiments, all the measurements were done in a closed Faraday cage and a conventional three-electrode system at the potential and the AC amplitude of 5 mV in the frequency range of 100 kHz to 0.1 Hz in the phosphate buffered saline (PBS) buffer (pH 7.4) containing 5×10^{-3} M $[Fe(CN)_6]^{3-4-}$ redox probe. The data was fitted with Randle's model (Figure 3e, inset) where R_S is the solution-phase resistance, C_{dl} is the double-layer capacitance, and Z_W is the Warburg impedance. According to the obtained Nyquist plots, a semicircular diameter of $R_{ct} \approx 1473.3\ \Omega$ was observed for the bare electrode and was increased to ≈1651.5 Ω after being modified by Bi_2Se_3 NPs which was deposited by Au for 10 min. This may have occurred due to the presence of Bi_2Se_3 NPs which slowed down the charge-transfer rate between the redox probe and Au electrode. After immobilization of the Bi_2Se_3@Au electrode with the thiolated-ssDNA (Bi_2Se_3@Au-ssDNA) the R_{ct} further increased to ≈1846.1 Ω due to the imposition of extra resistance to the electrode which decreased the charge-transfer rate between the interfaces and the solution also the negative backbone of the ssDNA might electrostatically repel the negatively charged redox probe ($Fe(CN)_6^{3-4-}$). The R_{ct} became greater to ≈2120.4 Ω upon the hybridization of the modified electrode with complementary DNA strand (Bi_2Se_3@Au-dsDNA). This may attributed to the poor conductivity of the nucleic acids as well as their intrinsic negative charge to hinder the electron transfer between the interfaces and the redox probe. Interestingly, when the Bi_2Se_3@Au-ssDNA electrode was hybridized by the 8 C-C mismatched complementary DNA in the presence of Ag^+ ion (Bi_2Se_3@Au-mDNA), the R_{ct} value increased slightly (≈1953.9 Ω) higher than the Bi_2Se_3@Au-ssDNA and lower than the Bi_2Se_3@Au-dsDNA showing the role of Ag^+ ion in the enhancement of charge-transfer rate between the redox probe and the modified electrode. Therefore, the obtained EIS results alternatively confirmed the structural formation of the Bi_2Se_3@Au-mDNA modified electrode.

2.3. Electrical Analysis of Bi_2Se_3@Au-mDNA Using Scanning Tunneling Microscopy (STM) and STS

To further investigate the morphology of the fabricated film in molecular level and also to study whether the Au deposition of Bi_2Se_3 NP affects the electrical properties of our TI NP, we conducted STM and STS at room temperature. The current–voltage (*I–V*) curves were measured while the tunneling current was being recorded by positioning the tungsten tip above the samples and swiping the tip-bias voltage from −3 to +3 V. A topographic image and the corresponding *I–V* curves of different production steps of our modified electrode are provided in **Figure 4**. Figure 4a–c shows the morphological images of Bi_2Se_3 NPs before and after being deposited by Au for 10 min, respectively. Considering their corresponding cross section curves, the vertical distance between the bare gold electrode surface and the Bi_2Se_3 NPs was 6.05 ± 1.1 and 6.35 ± 0.8 nm, respectively, illustrating that the Au was homogenously deposited onto the whole substrate. However, after Au deposition, the lateral size of the NPs were clearly expanded together with an increase in the roughness of the surface, demonstrating the successful Au deposition onto the NPs and gold surface. Figure 4d indicates the morphology of the Bi_2Se_3@Au-mDNA electrode. As seen in the magnified image and its corresponding cross section curves in Figure 4e, the mDNA was thoroughly immobilized onto the Bi_2Se_3 NPs and its vertical distance from Bi_2Se_3 NP and the bare gold electrode surface were calculated 7.38 ± 1.1 and 14.2 ± 0.9 nm, respectively.

A set of experiments was conducted to evaluate the *I–V* histograms of Bi_2Se_3, Bi_2Se_3@Au, and Bi_2Se_3@Au-mDNA electrodes. About 250 experimental curves were extracted from at least three similar *I–V* curves of different samples after the bare gold electrode signal subtraction. First, the Bi_2Se_3 NP absorbed onto the bare gold electrode was examined. As seen in Figure 4f (the black curve), a nonlinear *I–V* graph was observed which is due to the existence of the TI Bi_2Se_3 NPs. Interestingly, after Au deposition onto the Bi_2Se_3 NPs for 10 min (Bi_2Se_3@Au), the *I–V* curve almost remained unchanged but rotating a little counterclockwise, tending toward the linear state (the red curve). In order to make sure about the phenomena we increased the time of the Au deposition to 20 min and conducted STS measurement. As shown in Figure 4f (the blue curve), the *I–V* histogram obtained from the new modified electrode (Bi_2Se_3@Au^2) dramatically turned to the linear behavior and remained linear by increasing the Au deposition time (data are not shown). Also for the less than 10 min deposition time, no significant results were observed. The phenomena might be due to the intrinsic behavior of the TIs to have their surface states protected. Therefore, in case of the Bi_2Se_3@Au electrode, no band gap opening was observed thus the TI surface states might remain protected.[45] As schematically depicted in figure 4g, when the thickness of the deposited layer of Au exceeds from the certain amount, the electrons tend to travel through the lowest unoccupied energy states which is provided by the bare gold-Au clusters interface.[14] Figure 4h illustrates the *I–V* curve of Bi_2Se_3@Au-mDNA as a comparison with the Bi_2Se_3 NP. A wider *I–V* current was observed which can be resulted from the wider band gap of the nucleic acids (≈3 V) than the Bi_2Se_3 (≈2.3 V). As well, a slight shift toward the highest occupied molecule orbital of the mDNA can be attributed to the nonalignment and nonspecific binding sites of the two molecules of mDNA and Bi_2Se_3. For the comparison, the *I–V* behavior of mDNA (8 Ag^+ ion mediated dsDNA) on bare gold electrode, Bi_2Se_3@Au, and Bi_2Se_3@Au^2 was tested and the results are shown in Figure S3 (Supporting Information). The *I–V* curve of the Bi_2Se_3@Au- mDNA was negatively shifted in contrast with the mDNA on the bare gold electrode, whereas the Bi_2Se_3@Au^2-mDNA displayed a similar curve with the mDNA. This results further illustrated that the Bi_2Se_3 NPs did not have influence on the electrical properties of the electrode, when encapsulated with a thick layer of Au (Bi_2Se_3@Au^2). Nevertheless, the necessity for more accurate experiments to obtain the exact band gap and Dirac point variations in ultra-high vacuum state is highly acquired and would be an interesting research to be considered.

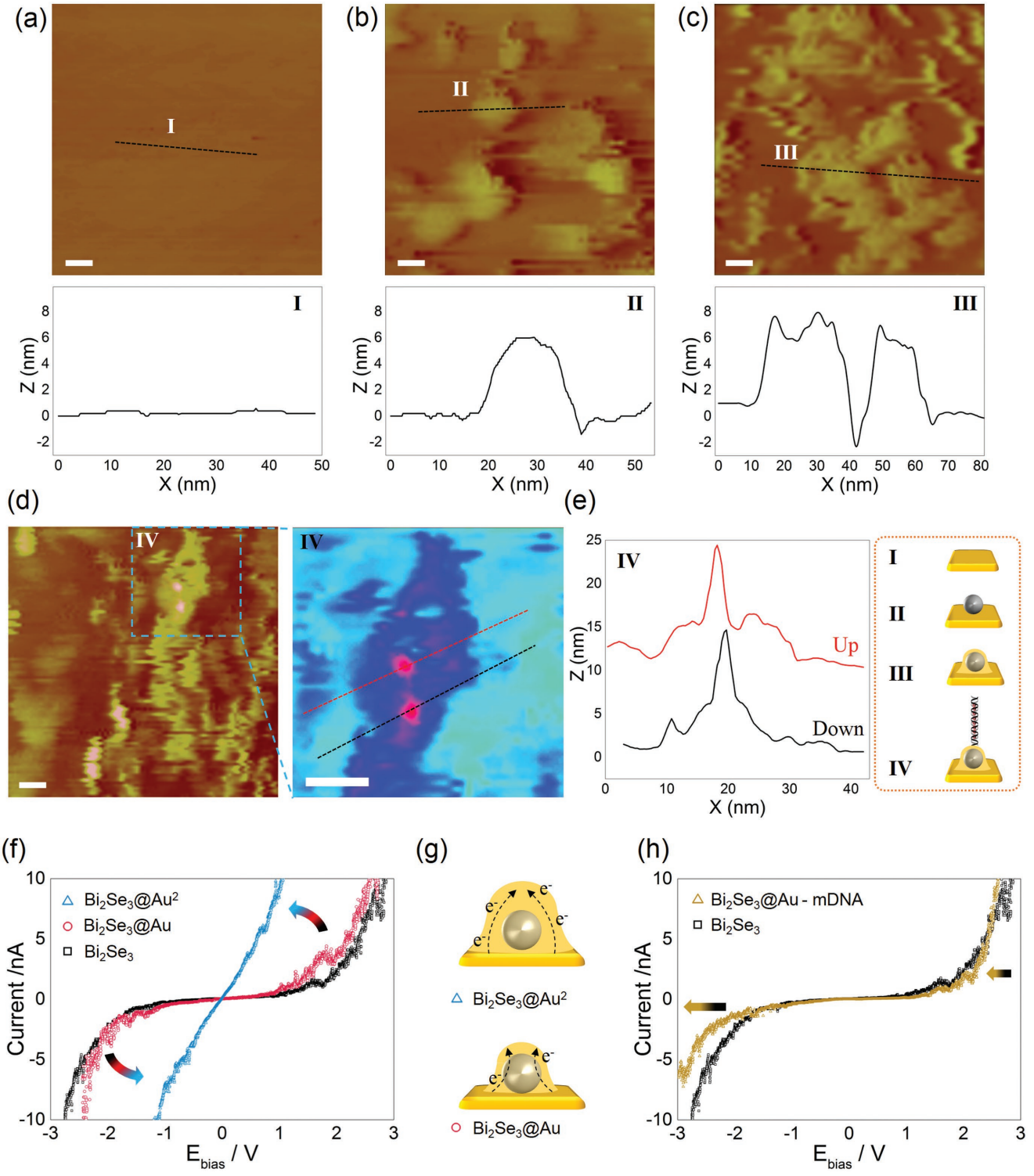

Figure 4. STM for morphological analysis of a) ultra-flat bare gold electrode, b) Bi_2Se_3, c) Bi_2Se_3@Au, and their corresponding cross section profiles at the bottom. d) Bi_2Se_3@Au-mDNA. e) Cross section profiles correspondent with the magnified image of Bi_2Se_3@Au-mDNA; the STM images were recorded in air with tunneling current of 1 nA and bias of 100 mV; scale bar is 10 nm. f) Current–voltage curves obtained from STS analysis at room temperature on Bi_2Se_3, Bi_2Se_3@Au (10 min Au deposition), and Bi_2Se_3@Au^2 (20 min Au deposition). g) Schematic diagram of electron migration from substrate to the STM tip. h) Current–voltage curves obtained from Bi_2Se_3@Au-mDNA electrode. The measurements are limited by a 1 GΩ series resistor. The measured DNA molecules were topographically scanned before and after *I–V* measurement, to confirm whether or not the structures remain intact and that the STM tip position was not changed.

2.4. Role of the Thin-Layer Au Deposition in the Electrochemical-Signal Stability of the Bi_2Se_3

To investigate the role of the Bi_2Se_3 on the electrochemical signal of the modified electrode, three sample sets of the bare gold electrode and the Bi_2Se_3 NPs immobilized onto the electrode before and after being sputtered by Au (called: Bi_2Se_3 and Bi_2Se_3@Au, respectively) were prepared and directed to the electrochemical cell under the same experimental conditions. Compared with the bare electrode, a dramatic increase of the electrochemical signal of the Bi_2Se_3-immobilized electrodes was evident (**Figure 5**a,b). The electrochemical signal, however, dropped after 20 CV cycles, and this is owing to the unstable physical adsorption of the Bi_2Se_3 NPs on the substrate and the subsequent wash-out and dissolution into the electrolyte solution. The third sample set, after the centrifuge NP self-assembly and the drying-out process, was placed into the thermal-evaporation system for 10 min in which the substrate was rotating at a constant angle of 30° to provide a homogenous thin layer of Au clusters onto the Bi_2Se_3-immobilized electrodes. Interestingly, these samples showed the very stable electrochemical signals, remaining approximately steady (relative standard deviation (RSD) ≈ 3.2%) after 20 CV cycles (Figure 5c). For the comparative analysis, the 20th cycle of each modified substrate was chosen and plotted in Figure 5d. Both, the role of the Bi_2Se_3 NPs on the electrochemical-signal enhancement of the bare electrode and the role of Au deposition process on the electrochemical-signal stability are quite evident. The achieved results further confirmed the remarkable feature of the TIs regarding the electrochemical-signal amplification.

2.5. CV Behavior of the Layer-by-Layer Self-Assembled Bi_2Se_3@Au-mDNA Film

The layer-by-layer self-assembly of the mDNA, having redox behavior, were investigated using CV technique in an N_2-saturated 10×10^{-3} M PBS buffer at a pH of 7.4 and the scan rate of 0.050 V s^{-1}. To compare the signals that were obtained from the different structures, a very small concentration of mDNA (1×10^{-12} M) with an optimized eight C-Ag^+-C modification (details in Section S.1 and Figure S4, Supporting Information) was assembled onto the surface. As shown in Figure S5 (Supporting Information) in the absence of the Ag^+, the standard potential of the ssDNA occurred at ≈326 ± 5 mV (E_{pc} ≈ 318 and E_{pa} ≈ 334), while it was measured at ≈269 ± 4 mV (E_{pc} ≈ 242 and E_{pa} ≈ 296) for the dsDNA. Figure 5e illustrates the CV behavior of the optimized 8 Ag^+ modified dsDNA (mDNA) immobilized on the bare gold and Bi_2Se_3@Au electrodes. Two pairs of quasi-reversible redox peaks that correspond to the DNA and Ag^+, respectively, from which the redox current peaks of both DNA and silver ion have been dramatically boosted when mDNA was immobilized onto the Bi_2Se_3@Au electrode. The DNA-redox potential was shifted and effectively separated, while very sharp

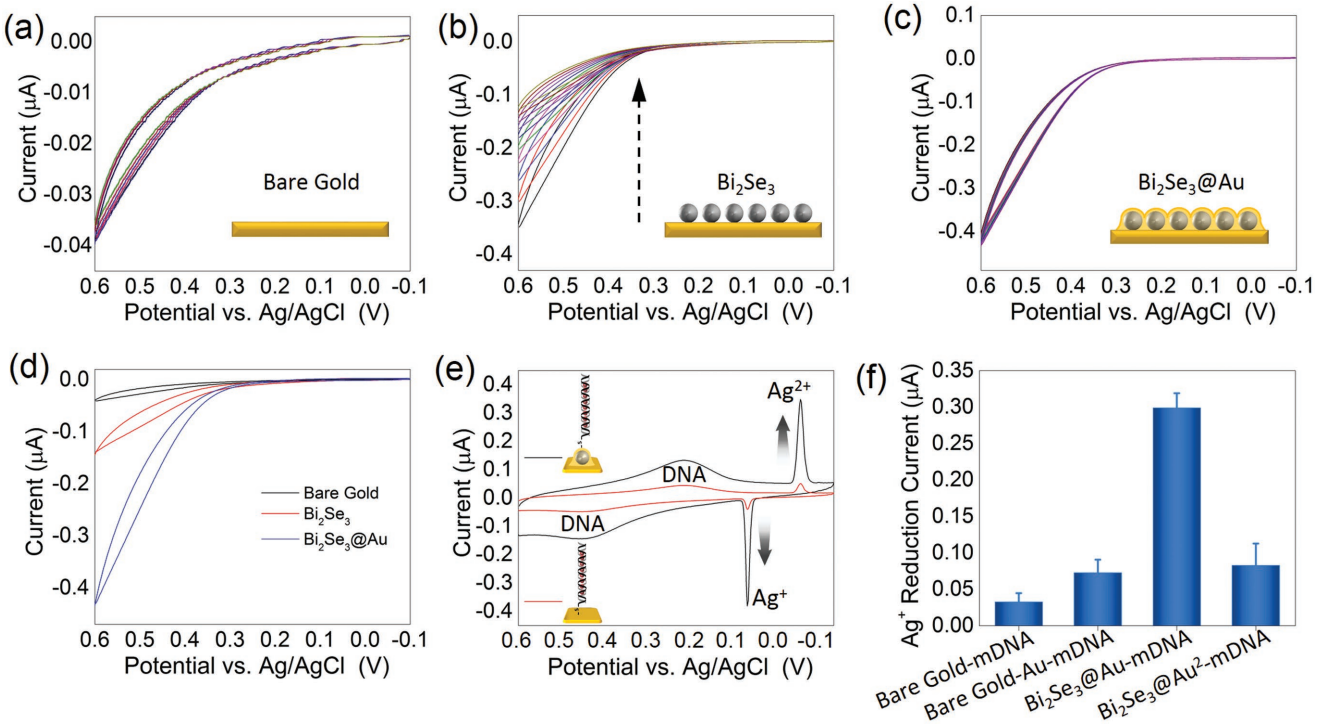

Figure 5. The role of Bi_2Se_3 on electrochemical-signal enhancement. 20 cycle of cyclic voltammograms (each 2 cycles' increments are shown) obtained from a) bare gold, b) Bi_2Se_3 before Au deposition, c) Bi_2Se_3 after Au deposition (Bi_2Se_3@Au). d) Comparison between the last 20th cycle of the three studied structures. e) Cyclic voltammograms obtained from bare gold-mDNA (red curve) and Bi_2Se_3@Au-mDNA (black curve); the DNA concentration was chosen 1×10^{-12} M in order to easily compare redox peaks of the species. f) Plotting the corresponding reduction peak of silver ion of mDNA immobilized onto the bare gold, bare gold after Au deposition, Bi_2Se_3@Au, and Bi_2Se_3@Au^2; statistical data were obtained from 15 independent samples fabricated in identical experimental conditions.

and distinctive redox-current peaks that resulted from Ag^+ reduction/oxidation were observed. The standard DNA potential was measured as ≈342 ± 6 mV (E_{pc} ≈ 232 and E_{pa} ≈ 452), and the reduction and oxidation potentials for the Ag^+ were observed at ≈–75 and ≈+54 mV, respectively, which corresponds to the Ag^+/Ag^{2+} redox activity of mDNA. Figure 5f shows the comparative statistical data of the silver ion reduction current obtained from the mDNA immobilized onto bare gold, bare gold after Au deposition, Bi_2Se_3@Au, and Bi_2Se_3@Au[2]. As seen, compared to the bare gold-mDNA, the bare electrode after being Au-deposited for 10 min and subsequent immobilization of mDNA showed higher reduction current of silver ion (≈2 times) because of the large surface area provided by the Au clusters. In case of the Bi_2Se_3@Au-mDNA, the reduction current of silver ion was enhanced by ≈10 times comparing to the result of the bare gold-mDNA. The results truly confirmed the effective immobilization of the mDNA on the modified electrode as well as the role of Bi_2Se_3@Au in the electrochemical-signal enhancement, also a controllable and efficient electron transfer between the mDNA and the Bi_2Se_3@Au substrate was revealed. The significant drop in the reduction current of mDNA immobilized onto the Bi_2Se_3@Au[2] electrode declared that the thickness of Au clusters has a big impact not only on the electrical behavior but also on the electrochemical behavior of the TI Bi_2Se_3 NPs. As a result, the Bi_2Se_3@Au-mDNA modified electrode was employed for the further experiments.

2.6. Analysis of the Redox Behavior of the mDNA and the Electron-Transfer Rate of the Bi_2Se_3@Au-mDNA Modified Electrode

The CV studies on the Bi_2Se_3@Au-mDNA were conducted in N_2-saturated 10×10^{-3} M PBS with a pH of 7.4 at different scan rates (υ), from 0.050 to 0.090 V s^{-1}. **Figure 6**a demonstrates that the increasing of the scan rate from 0.050 to 0.090 V s^{-1} led to a steady increase in the redox-current peaks. For both DNA and Ag^+, the cathodic- and anodic-peak potentials were also shifted gradually to the negative and positive sides, respectively (Figure 6a, insets). Linear relationships were observed between the redox-current peaks and the scan rate for both DNA and Ag^+, and they are plotted in Figure 6b. The above-mentioned result and the roughly symmetric redox-current peaks at the different scan rates confirmed a surface-controlled electrochemical electrode-based process.[46] From the linear relationship between the redox-peak currents of the Ag^+ and the square root of the scan rate ($\upsilon^{1/2}$) the regression equations of $i_{pc} = 0.192\ \upsilon^{1/2} - 1.346$ ($R^2 = 0.992$) and $i_{pa} = -0.2\ \upsilon^{1/2} + 1.407$ ($R^2 = 0.988$) can be derived (Figure 6c).

Plotting the cathodic- and anodic-potential peaks of the Ag^+ as a function of the log (υ) followed a linear fit that led to two straight lines (Figure 6d). The regression equations for the cathodic and anodic potentials are $E_{pc} = 2.602 \times 10^{-2} \log \upsilon + 5.8 \times 10^{-3}$ and $E_{pa} = -2.709 \times 10^{-2} \log \upsilon - 3.11 \times 10^{-2}$, respectively. Knowing that $k_c = -2.3RT/\alpha nF$ and $k_a = 2.3\ RT/(1-\alpha)nF$, in which k_c (0.02602) corresponds to the slope that is derived from

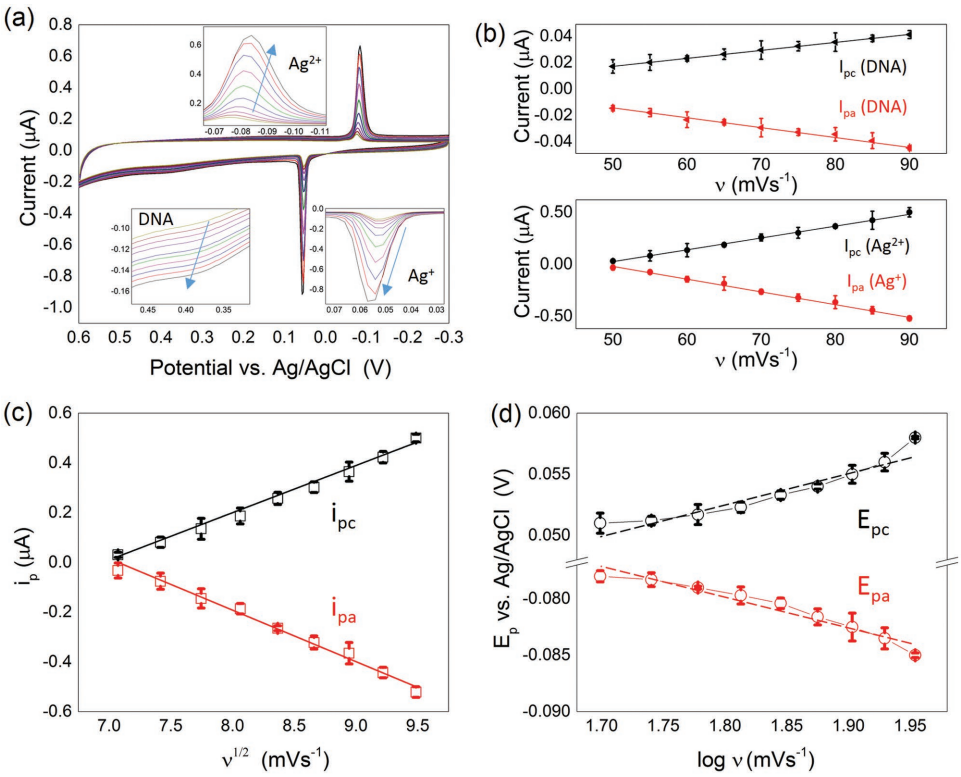

Figure 6. a) Cyclic voltammograms of Bi_2Se_3@Au-mDNA in 10×10^{-3} M PBS buffer (pH 7.4) with increasing scan rate (υ) from 0.05 to 0.09 V s^{-1}. b) Plot of the cathodic (i_{pc}) and anodic (i_{pa}) peak currents versus scan rate for DNA (upper curve) and silver ion (lower curve). c) The effect of log $\upsilon^{1/2}$ on the cathodic (i_{pc}) and anodic current (i_{pa}) of Ag^+ ion. d) The effect of log υ on the cathodic (E_{pc}) and anodic potential (E_{pa}) of mDNA.

$E_{pc} = f(\log \upsilon)$ and k_a (0.0271), corresponds to the slope that is deduced from $E_{pa} = f(\log \upsilon)$, and the following equation can be used[47]

$$\log \frac{k_a}{k_c} = \log \frac{\alpha}{1-\alpha} \tag{1}$$

Therefore, the charge-transfer coefficient value (α) was calculated as 0.511. In addition, according to the following equation, the apparent electron-transfer rate constant (k_s) between the mDNA and the Bi_2Se_3@Au substrate was determined as 0.71 s^{-1}.[47]

$$\log k_s = \alpha \log(1-\alpha) + (1-\alpha)\log\alpha - \log RT/nF\upsilon - \alpha(1-\alpha)nF\Delta E_p/2.3RT \tag{2}$$

where R is the gas constant, F is the Faraday constant, n is the number of electrons, and ΔE_p is the peak-to-peak separation ($\Delta E_p \approx 129$ mV) of the Ag^+-redox potentials (Ag^+/Ag^{2+}). The small ΔE_p value conveys a rapid electron-transfer rate, along with the presence of a negligible mass-transport effect between the mDNA and the modified substrate.

2.7. Electrochemical Detection of H_2O_2 Using the Bi_2Se_3@Au-mDNA Biosensor

The electrocatalytic reduction of the H_2O_2 on the Bi_2Se_3@Au-mDNA was verified using the CV and an amperometric (i–t) measurements. The possible chemical reaction for the electrochemical reduction of H_2O_2 is expressed in Equations (3) and (4). Since the occurrence of the redox-current peaks for the Ag^+ is more negative than that of the DNA peaks, the Ag^+ in the catalytic mechanism plays the dominant role, as follows

$$2Ag^+ + 2H^+ + H_2O_2 \xrightarrow{\text{yields}} 2Ag^{2+} + 2H_2O \tag{3}$$

$$Ag^{2+} + e^- \xrightarrow{\text{yields}} Ag^+ \tag{4}$$

The H_2O_2 effect on the cyclic voltammograms of the Bi_2Se_3@Au-mDNA is shown in **Figure 7**a. It is clear that, upon the concentration increment of the H_2O_2 from 0 to 35×10^{-3} M, a linear increase in the reduction (positive) and oxidation (negative) of the current peaks for both DNA and Ag^+ were observed, revealing a well electrocatalytic performance of the Bi_2Se_3@Au-mDNA electrode in response to the H_2O_2. The sensitivity, dynamic range, and detection-limit measurement were accurately examined using the amperometric (i–t) method.

For the amperometric analysis, a constant potential of – 0.1 V versus Ag/AgCl was chosen, where all of the species were in completely reduced states. In this regard, the Bi_2Se_3@Au-mDNA electrode was directed to the continuously stirred N_2-saturated 10×10^{-3} M PBS solution (pH 7.4), and the amperometric performance was recorded upon the addition of different H_2O_2 levels. Figure 7b shows a typical amperometric plot that is the result of the successive addition of 5 µL aliquots of H_2O_2 per 50 s from 0.10×10^{-6} M to 27.30×10^{-6} M. The concentration of the H_2O_2 titration was 100×10^{-9} M until 1.3×10^{-6} M was reached, at which point a change to 1×10^{-6} M increments occurred (Figure 7b, insets). A linear increase of the current response was seen upon the addition of the H_2O_2 with a regression equation of $I = 0.156$ C (µM) + 0.021; $R^2 = 0.997$ over a dynamic range of 0.10–27.30 $\times 10^{-6}$ M (Figure 7c). Also, a pronounced response time of 1.6 s was observed (Figure 7b, insets) which is lower than those of the previous reported modified electrodes (see Table S1, Supporting Information), and this clearly indicates a very fast electron transfer between the Bi_2Se_3@Au-mDNA substrate and the solution interface. The results certainly demonstrate that the Bi_2Se_3@Au-mDNA provides a rapid and well-proven response to the sequential addition of H_2O_2 with a long linear range. The sensitivity of the proposed biosensor from the slope of the regression equation/area of the electrode was measured as 1734.25 µA m M^{-1} cm^{-2}. Moreover, the detection limit was calculated 10.21×10^{-9} M ($\approx 10 \times 10^{-9}$ M) based on the $3 \times (S_b/m)$ method, where "S_b" is the standard deviation of the background current and "m" is the slope of the linear fitting curve.

We also compared the performance of the Bi_2Se_3@Au-mDNA biosensor with ferrous oxidation-xylenol orange assay. Pierce quantitative peroxide assay kit (aqueous) was used according to the manufacture's protocol. The hydrogen peroxide was serially diluted in the concentration range of 0.3–1000 $\times 10^{-6}$ M and the optical absorbance at 564 nm was measured for each aliquot. A wide dynamic range from 0.65×10^{-6} M to 100×10^{-6} M was observed (Figure S6, Supporting Information) whereas below the concentration of 0.65×10^{-6} M there was a considerable deviation between the obtained experimental results and the linear fitting curve ($R^2 = 0.557$, inset 2). The regression equation was $i_{pc} = 0.022$ C (µM) – $2.15e^{-5}$ ($R^2 = 0.991$) and the detection limit was measured 0.25×10^{-6} M. Although, the Pierce showed a wider dynamic range, the importance of the sensitivity of the H_2O_2 biosensor should not be neglected; for instance, the low concentrations of hydrogen peroxide can induce DNA lesions, cause many oxidative stresses, and affect viability of dermal fibroblasts (at the concentration of 16–32 $\times 10^{-9}$ M).[48,49] As a result, having an accurate linear dynamic range in the very low concentrations range would be demanding.

For a comparison, the capabilities of the bare-Au electrode and the Bi_2Se_3@Au electrode regarding the reduction of the H_2O_2 were also examined using the amperometric analysis. A volume of 5 µL of high-concentration H_2O_2 (10×10^{-3} M) was injected into 5 mL of 10×10^{-3} M PBS (pH 7.4), and the current responses of both electrodes were recorded. It is clear in Figure 7d that a very small increase of the current response of the bare electrode was observed, while it was higher in the case of the Bi_2Se_3@Au electrode, further confirming the role of the Bi_2Se_3 NPs in the electrochemical-signal enhancement of the bare-Au electrode. The responses, however, are both negligible and also very fast saturation time compared with the Bi_2Se_3@Au-mDNA electrode.

2.8. Selectivity and Stability Analysis of Bi_2Se_3@Au-mDNA Biosensor

The selectivity of the proposed biosensor was evaluated using different biological interfaces at 50 fold higher concentration than that of the H_2O_2. Uric acid, L-ascorbic acid, sodium

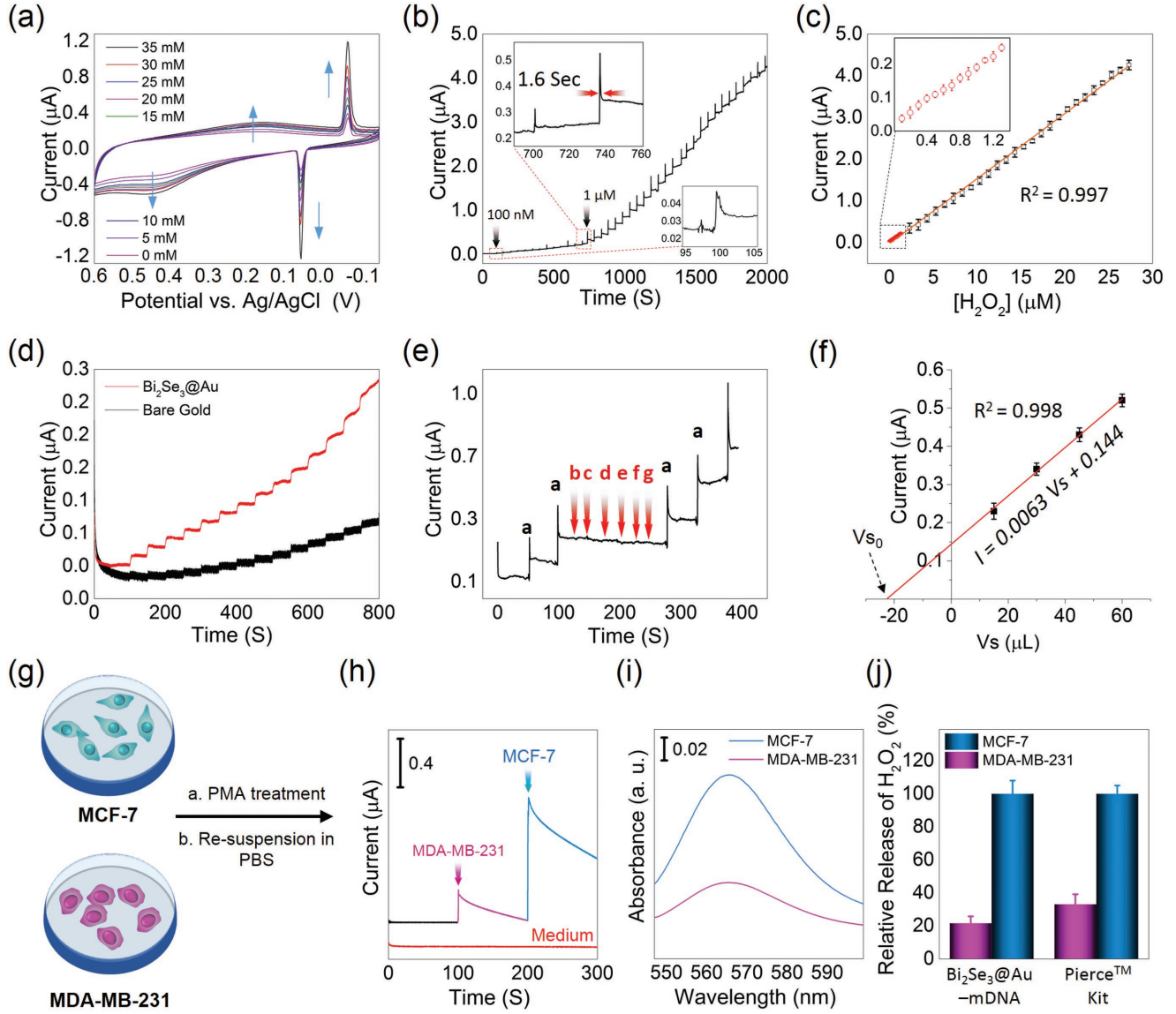

Figure 7. Sensor performance. a) Cyclic voltammograms of Bi_2Se_3@Au-mDNA in the absence and presence of H_2O_2 with different concentrations (0 to 35×10^{-3} M) at the scan rate of 50 mV s^{-1}. b) Amperometric response of the Bi_2Se_3@Au-mDNA upon successive addition of 5 μL aliquots of 0.1–27.3×10^{-6} M H_2O_2 to 5 mL stirred 10×10^{-3} M PBS buffer at pH 7.4 with an applied potential of –0.1 V under nitrogen atmosphere; upper inset shows the time of change in aliquot concentration from 100×10^{-9} to 1×10^{-6} M; lower inset shows the first injection of 100×10^{-9} M H_2O_2. c) Linear calibration curve of response current versus H_2O_2 concentration; inset shows the amplified curve at 0.1–1.3×10^{-6} M. d) Comparison between the current response toward 10×10^{-3} M addition of H_2O_2 for bare gold electrode and Bi_2Se_3@Au. e) Selectivity analysis of 5 μL addition of 1×10^{-6} M H_2O_2 (a) and 50×10^{-6} M uric acid (b), L-ascorbic acid (c), sodium nitrite (d), sodium bicarbonate (e), glucose (f), and sucrose (g). f) A typical standard addition curve for the detection of 1.0×10^{-6} M H_2O_2 in human serum; Vs_0 = 23.02 μL. g) Experimental scheme for the detection of H_2O_2 released from cancer cells. h) Typical amperometric response recorded at Bi_2Se_3@Au-mDNA biosensor after the addition of 10 μL solution of PMA-induced MDA-MB-231 (violate), PMA-induced MCF-7 (blue), and PMA-induced medium (red). i) Typical optical absorbance spectra obtained from Pierce kit measurement for PMA-induced MDA-MB-231 (violate) and PMA-induced MCF-7 (blue). j) The corresponding relative H_2O_2 released from the two cancer cell lines using both methods; data were obtained from three identical reactions.

nitrite, sodium bicarbonate, glucose, and sucrose were tested as the interfaces. As shown in Figure 7e, no remarkable current response was seen upon the addition of each analytes whereas the current response retained its value over the injection of H_2O_2. This data indicates the high selectivity of our Bi_2Se_3@Au-mDNA biosensor. Moreover, the stability test was carried out by monitoring the CV response of the Bi_2Se_3@Au-mDNA electrode over 80 cycles at the potential windows of 0.6 to –0.3 V and the RSD was measured 2.9% (Figure S7a, Supporting Information). Also, the reusability of the biosensor was tested after the storage of 3 weeks at 4 °C in which the current response to H_2O_2 sustained its 97% of the initial value (Figure S7b, Supporting Information). Moreover, after 3 weeks of storage, the electrochemical signal of the Ag^+ ion had a negligible drop after 80 CV cycles with the RSD of 3.4% (Figure S7b, inset, Supporting Information). Therefore, the prepared

Table 1. Detection of H_2O_2 in human serum using Bi_2Se_3@Au-mDNA biosensor.

Sample	Added [$\times 10^{-6}$ M]	Found [$\times 10^{-6}$ M]	Recovery [%]	RSD [%]
Serum 1	1.00	1.036	103.6	3.2
Serum 2	2.00	1.963	98.1	2.9
Serum 3	3.00	2.986	99.5	3.1

Bi_2Se_3@Au-mDNA biosensor exhibited a well stability and reusability performance.

2.9. Performance of the Bi_2Se_3@Au-mDNA Biosensor in Serum

To investigate the practical performance of the proposed biosensor, the Bi_2Se_3@Au-mDNA electrode was prepared and evaluated for the detection of H_2O_2 in serum. It should be mentioned that the mDNA showed good stability toward enzymatic degradation for 14 h together with high stability in different pH conditions (details in Section S.2 and Figure S8, Supporting Information). The H_2O_2 recovery in serum was monitored on the modified sensor using the standard addition method. Samples were diluted in a PBS buffer (pH 7.4) prior to the amperometric experiment. Later, H_2O_2 solutions were spiked into the electrolyte and the current responses were recorded. All of the measurements were performed in triplicate. A H_2O_2 recovery of 98.1% to 103.6% was observed for three different samples, suggesting the promising performance of the prepared sensor for the detection of H_2O_2 in a real sample (**Table 1**). Figure 7f illustrates a typical graph for the measurement of an unknown H_2O_2 concentration (1.0×10^{-6} M) in serum. By plotting the current response of the sensor as a function of the standard volume (*Vs*) and with the use of the following equation, the unknown H_2O_2 concentration in the serum can be calculated as follows[50]

$$C_x = -Vs_0 C_s / V_x \quad (5)$$

where C_x is the H_2O_2 concentration in the serum, C_s is the concentration of the standard solution (9×10^{-6} M), V_x is the constant volume of the sample aliquot (200 µL), and Vs_0 can be determined by the extrapolation of the fitting line back to the *Vs*-axis intercept where the current value is zero (23.02 µL).

2.10. Capability of the Bi_2Se_3@Au-mDNA Biosensor to Discriminate between Breast Cancer Cell Types

In order to further investigate the practical ability of our proposed biosensor in clinical samples, the extracellular H_2O_2 released from two human breast cancer cell lines (MCF-7 and MDA-MB-231) was measured and the results were compared with Pierce kit and previous studies. It was reported that, addition of PMA into the mentioned cancer cell solutions resulted in the cell stimulation followed by distinct extracellular generation of H_2O_2.[51,52] Inspired by that, same number of cells were used for both experiments (Bi_2Se_3@Au-mDNA biosensor and Pierce kit) which were previously harvested from the cultured media, treated with PMA (1 h) and resuspended in PBS (pH 7.4). The results is shown in Figure 7g–i. As shown in Figure 7h, upon the addition of PMA-induced MDA-MB-231 cells, an obvious current peak was observed, while, it was more intense in case of the PMA-induced MCF-7 cells. Also as the control experiment, the PMA was added into medium under identical conditions and no remarkable current change was observed. Similar results were obtained from the Pierce kit measurement in which the optical absorbance intensity arose from the PMA-induced MCF-7 cells was higher than that of the PMA-induced MDA-MB-231 cells. The level of H_2O_2 released from MDA-MB-231 and MCF-7 cells was measured on the basis of the standard curves obtained from both Bi_2Se_3@Au-mDNA biosensor and Pierce kit (Figure 7i). It can be clearly seen that, upon the identical conditions, the MCF-7 cells generated more extracellular H_2O_2 than the MDA-MB-231 cells, which is in consistence with the previous reports.[52] Notably, in the case of the Bi_2Se_3@Au-mDNA biosensor, the difference between the levels of H_2O_2 release was a bit higher than that of the Pierce kit. This may be attributed to the weakness of Pierce kit in the detection of low concentration of H_2O_2. As a result, we could successfully discriminate between two human breast cancer cell lines simply based on the difference between their H_2O_2 generations which has not been reported elsewhere.

3. Conclusion

In summary, a novel H_2O_2 biosensor was fabricated. Bi_2Se_3 NPs were centrifuge-assembled onto the gold electrode, prior to the further deposition by another thin layer of Au. Then, it was used as a solid substrate to receive mDNA (eight silver ions mediated dsDNA) through Au–S bonding and form Bi_2Se_3@Au-mDNA electrode. Owing to their unique electrical properties, the Bi_2Se_3 NPs facilitated an electron-transfer efficiency between the Au electrode and the mDNA, and they dampened the noise signals in addition to their provision of a large surface area for the enhancement of the electrocatalytic activity of the species, all of which resulted in an ultra-fast current response toward the H_2O_2 detection (1.6 s) and a very low detection limit of 10×10^{-9} M. For the first time we revealed that, the thickness of Au-deposited thin layer onto the Bi_2Se_3 NPs might have an important role in retrieving the exotic electrical and electrochemical properties of the TI Bi_2Se_3. The proposed cost-effective and simply designed H_2O_2 biosensor, which exhibited a high selectivity that is beyond those of other biological interfaces and a sound recovery in human serum could be further developed for the detection of different disease biomarkers. We also implemented a novel paradigm to electrochemically classify cancer cell subtypes based on the difference between their amount of H_2O_2 extracellular release (here breast cancer cells), which would be an interesting research topic for the classification and profiling the wide variety of cancer cells.

4. Experimental Section

The bare-Au electrode composed of an Au (50 nm)/Cr (2 nm)/SiO_2 layer with an active site of 9 mm^2 was provided by the National Nanofab Center (ROK). The grain-controlled ultra-flat Au substrate

(Platypus template-stripped gold chips) was purchased from Platypus Technologies (USA) for STM. L-ascorbic acid, uric acid, sodium nitrite ($NaNO_2$), sodium bicarbonate ($NaHCO_3$), glucose, sucrose, ethyle acetate, bovine serum albumin, bismuth (III) nitrate pentahydrate, triethanolamine, sodium selenosulfate solution, 6-mercaptohexanoic acid, PMA, and $AgNO_3$ were purchased from Sigma-Aldrich (USA). The H_2O_2 and the H_2SO_4 were purchased from Daejung Chemical (ROK). The dithiothreitol was prepared by Pierce (USA). Deionized water was purified using the Milli-Q system (Millipore, USA). The TEM grids were purchased from Ted Pella Inc. (USA). The Pierce Quantitative Peroxide Assay Kit (aqueous) was purchased from Thermo Scientific. The DNA strands were provided by Bioneer (ROK), and the sequences are listed in Section S.3 (Supporting Information). The Bi_2Se_3-synthesis procedure, the formation of the electrode substrates, the immobilization process of the mDNA onto the modified electrode surface, and the analysis techniques are also provided in Sections S4–S8 (Supporting Information). All of the electrochemical experiments were conducted using the CHI-660 potentiostat (CH Instruments, USA) and a three-electrode system (Section S.7, Supporting Information). The Nanoscope IV/Multimode AFM device (Digital Instruments, USA) was used to investigate the surface topography of the modified electrodes.

Supporting Information

Supporting Information is available from the Wiley Online Library or from the author

Acknowledgements

This research was supported by Leading Foreign Research Institute Recruitment Program through the National Research Foundation of Korea (NRF) funded by the Ministry of Science, ICT & Future Planning (MSIP) (2013K1A4A3055268), and by Basic Science Research Program through the National Research Foundation of Korea (NRF) funded by the Ministry of Education (2016R1A6A1A03012845) and by the Research Grant of Kwangwoon University in 2017.

Conflict of Interest

The authors declare no conflict of interest.

Keywords

bismuth selenide, cancer cells, electrochemical biosensor, extracellular hydrogen peroxide, topological insulators

Received: November 13, 2017
Revised: January 18, 2018
Published online:

[1] D. R. Thévenot, K. Toth, R. A. Durst, G. S. Wilson, *Biosens. Bioelectron.* **2001**, *16*, 121.
[2] J. Schalkwijk, W. B. van den Berg, L. B. van de Putte, L. A. Joosten, *Arthritis Rheum.* **1986**, *29*, 532.
[3] M. Rojkind, J.-A. Domínguez-Rosales, N. Nieto, P. Greenwel, *Cell. Mol. Life Sci.* **2002**, *59*, 1872.
[4] M. Tarvin, B. McCord, K. Mount, K. Sherlach, M. L. Miller, *J. Chromatogr. A* **2010**, *1217*, 7564.
[5] A. Brestovisky, E. KirowaEisner, J. Osteryoung, *Anal. Chem.* **1983**, *55*, 2063.
[6] D. Janasek, U. Spohn, *Sens. Actuators, B* **1997**, *39*, 291.
[7] K. Zhang, L. Mao, R. Cai, *Talanta* **2000**, *51*, 179.
[8] J. Nouroozzadeh, J. Tajaddinisarmadi, S. P. Wolff, *Anal. Biochem.* **1994**, *220*, 403.
[9] H. Liu, L. Weng, C. Yang, *Microchim. Acta* **2017**, *184*, 1267.
[10] G. A. M. El-Nagar, I. Derr, A. Fetyan, C. Roth, *Appl. Catal., B* **2017**, *204*, 185.
[11] W. Zhao, H. Wang, X. Qin, X. Wang, Z. Zhao, Z. Miao, L. Chen, M. Shan, Y. Fang, Q. Chen, *Talanta* **2009**, *80*, 1029.
[12] A. K. Yagati, T. Lee, J. Min, J.-W. Choi, *Colloids Surf., B* **2012**, *92*, 161.
[13] A. K. Yagati, T. Lee, J. Min, J.-W. Choi, *Bioelectrochemistry* **2011**, *80*, 169.
[14] M. Mohammadniaei, T. Lee, J. Yoon, D. Lee, J.-W. Choi, *Biosens. Bioelectron.* **2017**, *98*, 292.
[15] A. K. Yagati, T. Lee, J. Min, J.-W. Choi, *Biosens. Bioelectron.* **2013**, *47*, 385.
[16] I. L. de Mattos, L. Gorton, T. Laurell, A. Malinauskas, A. A. Karyakin, *Talanta* **2000**, *52*, 791.
[17] J. Wang, *Electroanalysis* **2005**, *17*, 7.
[18] E. B. Bahadır, M. K. Sezgintürk, *TrAC, Trends Anal. Chem.* **2016**, *76*, 1.
[19] R. Yoshimi, A. Tsukazaki, K. Kikutake, J. G. Checkelsky, K. S. Takahashi, M. Kawasaki, Y. Tokura, *Nat. Mater.* **2014**, *13*, 253.
[20] J. E. Moore, *Nature* **2010**, *464*, 194.
[21] A. R. Mellnik, J. S. Lee, A. Richardella, J. L. Grab, P. J. Mintun, M. H. Fischer, A. Vaezi, A. Manchon, E. A. Kim, N. Samarth, D. C. Ralph, *Nature* **2014**, *511*, 449.
[22] B. A. Bernevig, T. L. Hughes, S.-C. Zhang, *Science* **2006**, *314*, 1757.
[23] L. Fu, C. L. Kane, *Phys. Rev. B* **2007**, *76*, 045302.
[24] M. König, S. Wiedmann, C. Brüne, A. Roth, H. Buhmann, L. W. Molenkamp, X.-L. Qi, S.-C. Zhang, *Science* **2007**, *318*, 766.
[25] P. Di Pietro, M. Ortolani, O. Limaj, A. Di Gaspare, V. Giliberti, F. Giorgianni, M. Brahlek, N. Bansal, N. Koirala, S. Oh, P. Calvani, S. Lupi, *Nat. Nanotechnol.* **2013**, *8*, 556.
[26] K. Kadel, L. Kumari, W. Li, J. Y. Huang, P. P. Provencio, *Nanoscale Res. Lett.* **2010**, *6*, 57.
[27] J. Guozhi, W. Peng, Z. Yanbang, C. Kai, *Sci. Rep.* **2016**, *6*, 25884.
[28] D. Hsieh, Y. Xia, D. Qian, L. Wray, F. Meier, J. H. Dil, J. Osterwalder, L. Patthey, A. V. Fedorov, H. Lin, A. Bansil, D. Grauer, Y. S. Hor, R. J. Cava, M. Z. Hasan, *Phys. Rev. Lett.* **2009**, *103*, 146401.
[29] J. Stankiewicz, P. F. S. Rosa, P. Schlottmann, Z. Fisk, *Phys. Rev. B* **2016**, *94*, 125141.
[30] J. Li, F. Jiang, B. Yang, X.-R. Song, Y. Liu, H.-H. Yang, D.-R. Cao, W.-R. Shi, G.-N. Chen, *Sci. Rep.* **2013**, *3*, 1998.
[31] X.-D. Zhang, J. Chen, Y. Min, G. B. Park, X. Shen, S.-S. Song, Y.-M. Sun, H. Wang, W. Long, J. Xie, K. Gao, L. Zhang, S. Fan, F. Fan, U. Jeong, *Adv. Funct. Mater.* **2014**, *24*, 1718.
[32] S. Wu, G. Liu, P. Li, H. Liu, H. Xu, *Biosens. Bioelectron.* **2012**, *38*, 289.
[33] S. Chen, Y.-M. Fang, J. Li, J.-J. Sun, G.-N. Chen, H.-H. Yang, *Biosens. Bioelectron.* **2013**, *46*, 171.
[34] L. Xiao, A. Zhu, Q. Xu, Y. Chen, J. Xu, J. Weng, *ACS Appl. Mater. Interfaces* **2017**, *9*, 6931.
[35] P. Roushan, J. Seo, C. V. Parker, Y. S. Hor, D. Hsieh, D. Qian, A. Richardella, M. Z. Hasan, R. J. Cava, A. Yazdani, *Nature* **2009**, *460*, 1106.
[36] M. Z. Hossain, S. L. Rumyantsev, D. Teweldebrhan, K. M. F. Shahil, M. Shur, A. A. Balandin, *Phys. Status Solidi A* **2011**, *208*, 144.
[37] D. Kong, J. C. Randel, H. Peng, J. J. Cha, S. Meister, K. Lai, Y. Chen, Z.-X. Shen, H. C. Manoharan, Y. Cui, *Nano Lett.* **2010**, *10*, 329.
[38] H. Peng, W. Dang, J. Cao, Y. Chen, D. Wu, W. Zheng, H. Li, Z.-X. Shen, Z. Liu, *Nat. Chem.* **2012**, *4*, 281.
[39] J. J. Cha, K. J. Koski, Y. Cui, *Phys. Status Solidi RRL* **2013**, *7*, 15.
[40] H. Zhu, C. A. Richter, E. Zhao, J. E. Bonevich, W. A. Kimes, H.-J. Jang, H. Yuan, H. Li, A. Arab, O. Kirillov, J. E. Maslar, D. E. Ioannou, Q. Li, *Sci. Rep.* **2013**, *3*, 1757.

[41] J. Yoon, T. Lee, B. Bapurao G, J. Jo, B.-K. Oh, J.-W. Choi, *Biosens. Bioelectron.* **2017**, *93*, 14.
[42] H. Liu, X. Su, C. Duan, X. Dong, Z. Zhu, *Mater. Lett.* **2014**, *122*, 182.
[43] H. Fan, S. Zhang, P. Ju, H. Su, S. Ai, *Electrochim. Acta* **2012**, *64*, 171.
[44] A. Ono, S. Cao, H. Togashi, M. Tashiro, T. Fujimoto, T. Machinami, S. Oda, Y. Miyake, I. Okamoto, Y. Tanaka, *Chem. Commun.* **2008**, *39*, 4825.
[45] M. R. Scholz, J. Sánchez-Barriga, D. Marchenko, A. Varykhalov, A. Volykhov, L. V. Yashina, O. Rader, *Phys. Rev. Lett.* **2012**, *108*, 256810.
[46] K.-J. Huang, X. Liu, W.-Z. Xie, H.-X. Yuan, *Colloids Surf., B* **2008**, *64*, 269.
[47] E. Laviron, *J. Electroanal. Chem. Interfacial Electrochem.* **1979**, *101*, 19.
[48] A. T. Wright, T. Magnaldo, R. L. Sontag, L. N. Anderson, N. C. Sadler, P. D. Piehowski, Y. Gache, T. J. Weber, *Mol. Carcinog.* **2015**, *54*, 473.
[49] J. Nakamura, E. R. Purvis, J. A. Swenberg, *Nucleic Acids Res.* **2003**, *31*, 1790.
[50] G. R. Bruce, P. S. Gill, *J. Chem. Educ.* **1999**, *76*, 805.
[51] P. Wu, Z. Cai, Y. Gao, H. Zhang, C. Cai, *Chem. Commun.* **2011**, *47*, 11327.
[52] A. Damianaki, E. Bakogeorgou, M. Kampa, G. Notas, A. Hatzoglou, S. Panagiotou, C. Gemetzi, E. Kouroumalis, P.-M. Martin, E. Castanas, *J. Cell. Biochem.* **2000**, *78*, 429.